Multi-walled carbon nanotubes photochemistry: A mechanistic view of the effect of impurities and oxygen-containing surface groups

Damián Rodríguez Sartori [a], María Laura Dell'Arciprete [a], Giuliana Magnacca [b], Paola Calza [b], Enzo Laurenti [b], Mónica C. Gonzalez [a, *]

[a] Instituto de Investigaciones Fisicoquímicas Teóricas y Aplicadas (INIFTA), CCT-La Plata-CONICET, Universidad Nacional de La Plata, Diagonal 113 y 64, La Plata, Argentina
[b] Dipartimento di Chimica, and NIS Inter-Departmental Centre, Università di Torino, Via Giuria 7, Torino, Italy

ARTICLE INFO

ABSTRACT

Continuous photolysis experiments and transient absorption spectroscopy were performed in combination with other techniques including HRTEM, XPS, Raman, TGA, and ESR spectroscopy, to investigate the role of residual metals and amorphous carbon on the photochemical process taking place after 350–355 nm light irradiation of as obtained commercial multi-walled carbon nanotubes, denoted as pCNT.

The results indicate that 350–355 nm photolysis of pCNT leads to the oxidation of surface oxygen-containing groups and defects which in turn are eliminated leading to more graphitic –like multi-walled carbon nanotubes (MWCNT). Residual metal catalysts and oxygen containing amorphous carbon and oxidized C-functionalities of MWCNT play an important role in the generation of MWCNT photoinduced charge-separated states. The process of 350 nm excitation of pCNT leads to exciton formation followed by hole transfer to metal oxides and further oxidation of C-O functionalities. A plausible mechanism explaining the elimination of oxidized groups attached to pCNT graphene walls and amorphous carbon and leading to more graphite-like CNTs is discussed. The results presented may have implications in the nanoscale semiconductor materials for optoelectronics applications.

© 2018 Elsevier Ltd. All rights reserved.

1. Introduction

Because of their excellent electrical, optical, and chemical properties, multi-walled carbon nanotubes (MWCNT) are being vastly used in a broad range of applications within the medical, technological, and environmental sectors with the consequent production reaching the millions of tons [1]. MWCNT electronic properties and the number of defects at the edges and plane sites are influenced by the way in which the graphite sheets are rolled up in concentric tubes. Defects play a major role and can even dominate the physical and chemical properties of MWCNT [2]. Most popular synthetic methods produce a mixture of MWCNT of various diameters and chiralities usually contaminated with metallic catalysts (iron/graphite, cobalt/graphite, and iron/silica, among others) and amorphous or graphitic carbon [1–3]. Residual metals are difficult to remove [4] and it is nowadays recognized that they may alter the electronic and electrochemical properties of MWCNT [5,6].

Light irradiation has long been recognized to induce strong effects on carbon nanotubes morphology as evidenced in the Raman spectrum obtained with different wavelengths and power density of the excitation laser [7,8]. Among the different effects reported in the literature are: the loss of impurities, induction of defects, and the irreversible destruction of MWCNT and single wall carbon nanotubes (SWCNT). In particular, SWCNT photolysis with 266 nm light in N_2 atmosphere develops very high temperature and pressure [9] leading to the total melting and amorphization of the material with the increase in the laser fluence and pulse accumulation. UV light was also reported to accelerate SWCNT oxidation and cross-linking involving light-generated surface radicals and solvent molecules [10]. Despite most work has been reported for well controlled and purified SWCNT, little is known on the UVA-visible light effect on as-obtained commercial MWCNT which are the most widely used for industrial applications.

Herein, we report the effect of lamp irradiation with light of 350 nm of commercial pristine MWCNTs (pCNTs) in an attempt to understand the effect of metallic impurities and surface functional groups on the radical formation capacity of these materials. Lamp

* Corresponding author.
E-mail address: gonzalez@inifta.unlp.edu.ar (M.C. Gonzalez).

irradiation avoids the occurrence of possible multiphoton absorption processes frequently taking place with intense lasers. However, to obtain information on the chemical processes initiating light-induced morphological changes, time resolved photochemical experiments were performed with a laser flash photolysis equipment using the third harmonic of a Nd-YAG laser under conditions where mainly one photon processes are observed.

2. Experimental methods

The list of reactants and the standard equipment used (FTIR, IR-ATR, XRD, HRTEM, XPS, TGA, ICP, magnetization curves, and UV-vis and Raman spectrometers) are described in the supporting data (S.D. Reactants and Equipment, respectively). In particular, Commercial MWCNTs, here denoted as pCNTs, were NanocylTM NC7000 Industrial grade, C purity 90%, Diameter 9.5 nm, Length 1.5 μm, Specific Surface Area 475 $m^2 g^{-1}$. Published content of main impurities determined by EDX analysis: Al (5.9 wt%) Fe (0.5 wt%), and Co (0.2 wt%).

2.1. Sample preparation and purification

Purification of pCNTs by HCl. Briefly, 1g of pCNTs were dispersed in 200 mL 12M HCl and left stand for 5 h under continuous stirring at room temperature. The purified MWCNT, denoted as HCltCNTs, were filtered with 0.45 μm membranes and washed several times with deionized water, dried at 80 °C under vacuum, and stored in dark-colored flasks.

Photolyzed pCNTs: To observe changes in the morphology and characteristics of UVA lamp-photolyzed pCNTs, *ca.* 200 mL of an aqueous suspension containing 10 mgL^{-1} of pCNT were inmersed in a tubular quartz reactor and laterally irradiated for 20 h with 350 nm light from eight Rayonet lamps (Southern N.E. UltravioletCo.). The light incident intensity on the reactor cell was of 3.3×10^{-5} einstein/s. Irradiated suspensions were filtered with 0.45 μm membranes and the filtrate solids, denoted iCNTs, were washed several times with deionized water, dried at 80 °C under vacuum, and stored in dark-colored flasks.

2.2. Equipment and methods

The metal content of the particles was measured by ICP-AES after acid digestion of the MWCNTs. To that purpose, *ca.* 65 mg of pCNT were suspended in a 1:3 solution of concentrated HNO$_3$ and HCl acids contained in a Teflon reactor. The system was heated for 30 min with a standard microwave program, cooled at room temperature and filtered. The remaining filtrate was further diluted with milliQ water to a final volume of 40 mL. Signals were calibrated against standard metal solutions.

Laser Flash Photolysis Experiments (LFP) were performed at 25 ± 2 °C with standard equipment described in the S.D. A pulse of 355 nm light was used to excite 2 mL of aqueous suspensions containing 10 ppm of either pCNT, HCltCNT, or iCNTs contained in a 1 cm path light quartz cuvette. To avoid deterioration of MWCNT, fresh sample is continuously exposed to the laser pulse.

EPR experiments were performed at 25 ± 2 °C with standard equipment described in the S.D. All experiments were carried out by adding the spin trap in the cell before irradiating and the EPR spectra were acquired immediately after the irradiation. To that purpose, 5 mL of an aqueous suspension containing 10 ppm of pCNT were mixed with the spin trap and the mixture irradiated for 5 min. Irradiation was performed with a 550W Xenon short arc lamp with an incident photon rate over the 280–550 nm range. Either 5-(diethoxyphosphoryl)-5-methyl-1-pyrroline-N-oxide (DEPMPO, 5 mM) and 5,5–dimethyl-1-pyrroline-N oxide (DMPO,

17.4 mM) were employed as trapping agent for O$_2$·$^-$ and HO·, respectively.

Hydrogen peroxide determination: [H$_2$O$_2$] was measured by an enzymatic colorimetric method employing the commercial kit Colestat for cholesterol quantification, Wiener Lab Argentina. Calibration curves were performed using standard H$_2$O$_2$ commercial solutions. To that purpose, 2 mL of a 10 ppm aqueous suspensions of either pCNT, HCltCNT, or iCNT were photolyzed for 60 min in a quartz cell with light of 350 nm from a Rayonet lamp to allow for H$_2$O$_2$ accumulation. The irradiated suspension was filtered and 0.4 mL of the filtrate were added to 1.8 mL of Colestat reactant, the mixture was allowed to react at 37 °C for 5 min and the absorbance at 505 nm was measured.

The software application called Glotaran [11], free edition, was used as a tool for global and target analysis of time-resolved spectroscopy data.

3. Results and discussion

3.1. Irradiation experiments with lamps

Continuous irradiation experiments were performed to observe the effects of light on pCNT. Several methods were used to obtain a detailed characterization of pristine (pCNT) and light irradiated pCNT (denoted as iCNT). Treated pCNT with HCl to reduce the metal content, HCltCNT, were used as a control when required.

The first-order Raman spectra of pCNT and iCNT show the characteristic sharp Raman peaks of MWCNT: (*i*) the weakly asymmetric G-band at ~1580 cm^{-1} of graphitic layers related to the lattice vibration of all carbon materials with sp2 bonds and (*ii*) the dispersive D and D' modes at about 1350 and 1620 cm^{-1}, respectively, with defect-dependent intensities [12]. The D band activated by the presence of disorder in carbon systems [7] has been related to the presence of amorphous carbon in double-walled CNT studies [13,14] while the D' mode has been associated with disorder introduced by functionalization and strain of graphite-like materials [15]. Comparison of the area of the D and G peaks, A_D/A_G (Fig. 1A), is widely accepted to give information on the structural quality of nanotubes. pCNT show larger A_D/A_G (1.5 ± 0.1) than iCNT (0.8 ± 0.1) thus indicating that defective nanotubes and/or amorphous carbon are partially removed after 350 nm irradiation [12,16].

Both powder X-ray diffraction patterns of pCNT and iCNT, see Fig. 1B, show a broad peak centered at $2\theta = 26.0°$ with similar width at half height but of different height. This behavior suggests that the peak is formed by the superposition of a broad and weak amorphous C peak (low angle side) and a sharp (002) graphitic peak at 26.5°, which corresponds to an interlayer graphitic lattice spacing of 0.335 nm. NiO (200) diffraction pattern at 43.2° (JCPDS card no. #47–1049) is also observed in both samples.

The FTIR spectrum of pCNTs (see curve *a* in Fig. 2A) shows important absorption bands at 3440, 2925, and 2860 cm^{-1} attributed to OH stretching and asymmetric and symmetric CH stretching, respectively. Peaks at 1640, and 1540 cm^{-1} may be assigned to conjugated C=C stretching and aromatic bending, respectively. In fact, bands *ca.* 1550 and 1200 cm^{-1} have been related to the G and D bands observed in the Raman spectra [14]. The small peak observed at 1445 cm^{-1} has been identified as unique to MWCNT [14]. Peaks at 1391 and 1097 cm^{-1} are attributed to C–O stretch in alcohols and phenols, respectively. The presence of C–O containing functional groups may have being introduced during the production processes and by atmospheric moisture [17]. However, the contribution of Si–O stretching vibrations in the 1050–1100 cm^{-1} region may not be discarded considering that SiO$_2$ is present as residual impurity. Peaks around 1740 cm^{-1}, assigned to stretching vibrations of
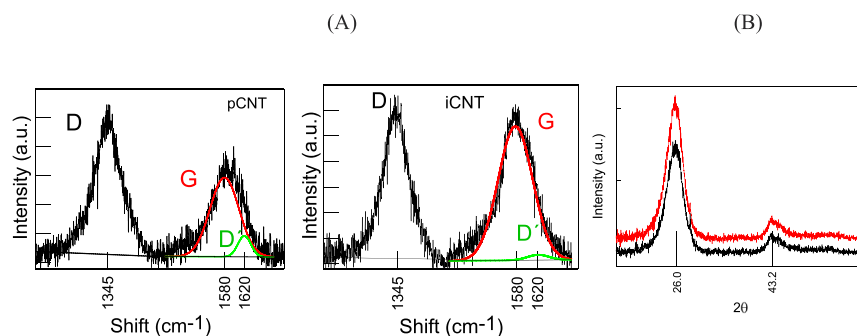
Fig. 1. (A) First order Raman spectrum of pCNT and iCNT. (B) X-ray diffraction spectra of (from down to top) pCNT and iCNT. (A colour version of this figure can be viewed online.)
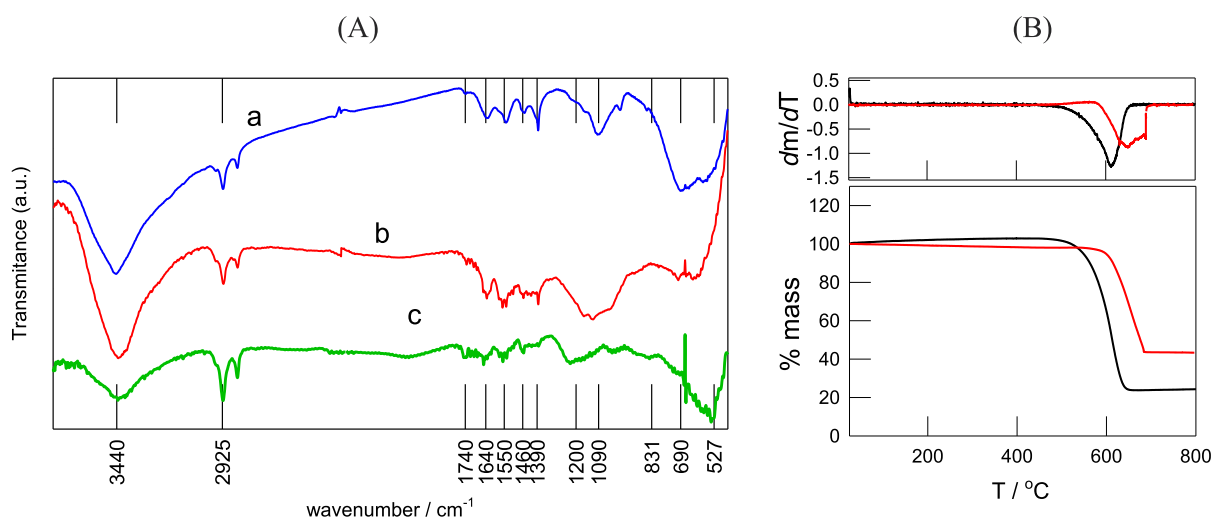

Fig. 2. (A) FTIR spectrum of (*a*) pCNT, (*b*) HCl-tCNT, (*c*) iCNT. (B) TGA curves and corresponding derivatives of pCNT (black) and iCNT (red) in an oxygen atmosphere. (A colour version of this figure can be viewed online.)

carbonyl groups (C=O) present in carboxylic acids are of little significance. The broad intense bands in the 680—540 cm^{-1} range may be due to metal oxides used in the synthesis process, as magnetite and iron oxides showing characteristic bands in the 630 - 572 cm^{-1} region. In fact, the spectrum of HCltCNT (see curve *b* in Fig. 2A) do not show significant peaks attributed to metal oxides while characteristic peaks due to surface-oxidized MWCNT are still of importance, in agreement with the reduced metal content of these materials. Interestingly, FTIR spectrum of iCNT samples, curve *c* in Fig. 2A, show depleted C—O and H—O signals when compared to those of CH stretching, thus supporting a lower content of oxygen-containing surface groups after irradiation. Peaks assigned to metal oxides in the 690—500 cm^{-1} region are still observed.

Thermogravimetric analysis curves (TGA) and their corresponding derivatives are shown in Fig. 2B. TGA performed for pCNT in air atmosphere shows an oxidation temperature of 610 °C at the point of maximum weight loss and a final residual mass of 24% attributed to oxidized metals [18]. On the other hand, iCNT show several oxidation processes occurring in the range from 610 to 685 °C, denoted by a large peak in the derivative curve. MWCNTs oxidation processes typically occur in the range from 400 to 650 °C; any modification caused by surface functionalization, introduction of defect sites, and shortened lengths are reported to decrease the oxidation temperature [14]. Therefore, the higher oxidation temperatures observed for iCNT samples suggest the formation of more resistant to oxidation components after light irradiation [17]. XRD

analyses of TGA residues of iCNT shows the presence of small peaks at 2θ *ca.* 35.5, 43, 47, 63.2, and 67, see S.D. XRD, attributed to Fe_2O_4, NiO, and Co_2O_3 thus evidencing that TGA residues are mainly due to metal oxides. It is almost surprising that the residual mass observed for iCNT is much higher than that of pCNT (24 *vs.* 40%, respectively). However, as will be discussed later in the text, HRTEM micrographs suggest that irradiation causes a carbon loss due to the light-induced pealing, thus inducing an enrichment in metals in the iCNT sample leading to the consequent increase of the TGA residue amount.

TEM micrographs of pCNT, see Fig. 3, show characteristic images of MWCNT bundles of *ca.* 12 nm wide tubes with mostly closed ends and the presence of amorphous material. iCNT micrographs, see Fig. 3, also depict characteristic images of MWCNT bundles. However, differing features from those of pCNT are the presence of crystalline, non-tubular entities of varying size and spiral-like graphitic structures, as shown in Fig. 3. Non tubular crystalline entities show plane spacing of 0.335 nm (corresponding 2θ values of 26.5 in XRD, *vide supra*), of the order of the inter-shell spacing between graphene sheets [19]. It is highly probable that the crystalline graphitic material is formed from broken pCNT as suggested by the presence of thinner tubes in some iCNT images, see S.D HRTEM. However, the high agglomeration observed in these TEM micrographs prevents the performance of a statistical analysis determining the higher number of iCNT bundles <12 nm wide and/ or of shorter length compared to pCNT.
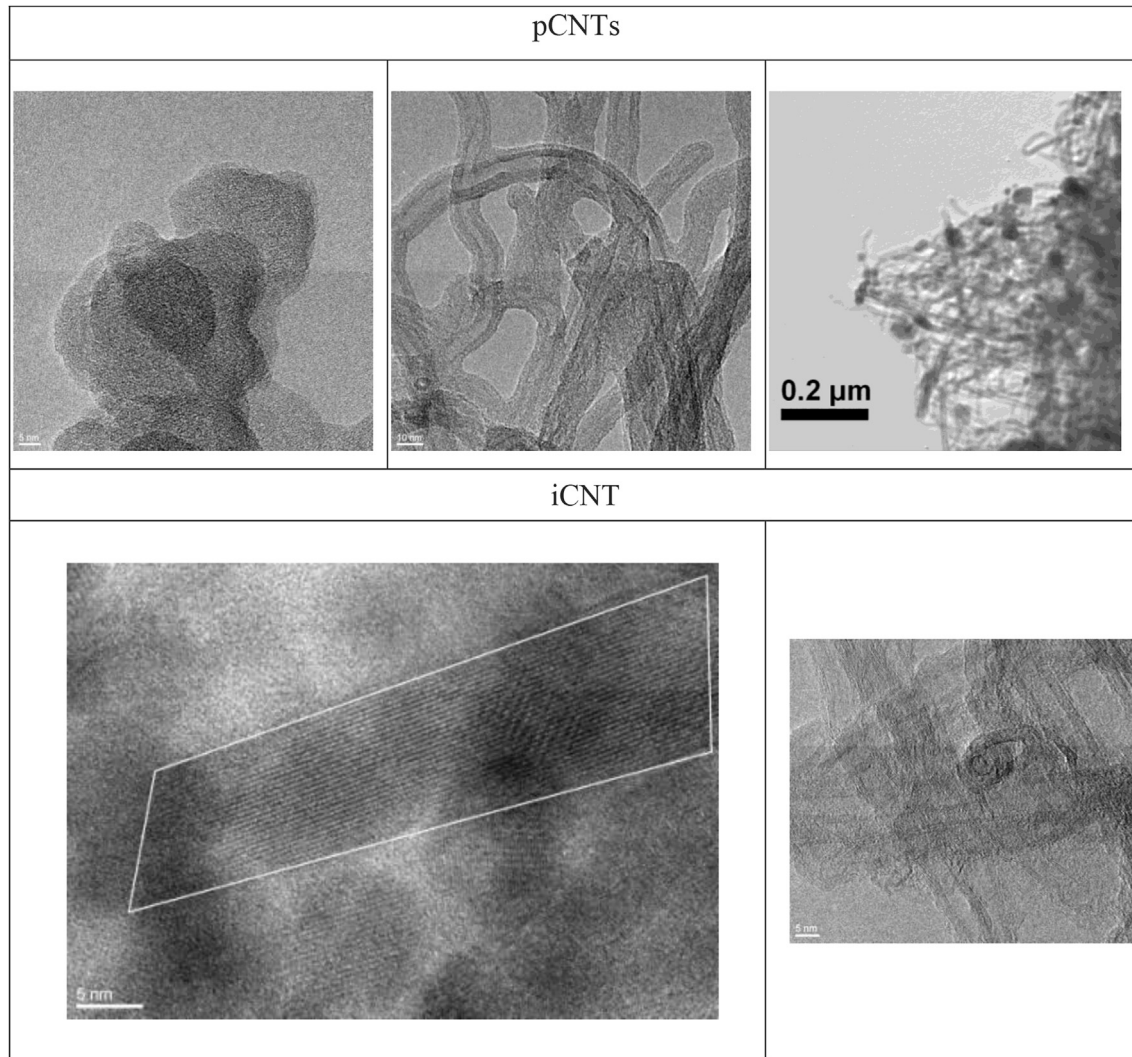
Fig. 3. TEM and HRTEM micrographs of pCNT and iCNT. White lines highlight graphitic entities.

EDS analysis of pCNT suggest the presence of Fe, Co, Al, and Si, see S.D. EDS. However, not all the metals are in the external side of pCNTs available for reaction and interaction with suspension components. XPS analysis of pCNT samples on a silicon support shows the presence of traces of Fe, Co, and Al at the MWCNT external surface. Argon etching of pCNT inside the XPS sample chamber allows the observation of metals located within the interior of the MWCNT. Fe and Co increase with etching time and Ni is observed only after etching, as depicted in Fig. 4.

The Al 2p3/2 band at 75,5 eV and spaced by 0.44 eV from that of p1/2 (see S.D. XPS) agrees with those of alumina coated graphite [19] and with aluminum oxide/hydroxide films. Nonetheless, a detailed analysis is misleading since Si satellites are superposed to Al signals.

Ni is located deep in the inner part of pCNTs, as well as Fe and Co. However, minor quantities of Fe and Co are also observed in pCNT surface. In the inside, Fe is present as Fe^0 and FeO as suggested by the 2p3/2 characteristic peaks at 707 and 710 eV, respectively; separated by 12.7 eV from the corresponding 2p1/2 spin-orbit components, see Fig. 4. In the outer part, Fe traces are oxidized, as mainly peaks at 710 eV are observed. Co 2p region shows a complex feature of peaks prevailing those at 778.9 (asymmetric), 781.5, and 784–787 eV characteristic of metallic Co,

CoO, and Co(II) satellite, respectively. Ni 2p3/2 peaks at 853.2 eV with split spin-orbit components 2p1/2 at 870.6 eV and satellites at 859.2 and 875.6 eV are characteristic of metallic Ni [20].

The C1s XPS band of pCNT, see Fig. 4, shows the contribution of peaks at 284.5, 285.2, 287.1, 289.1 and 291 eV, in line with literature reports [21,22]. Bands with binding energies (BE) of 287.1, 289.1 and 291 eV are assigned to carbon atoms bound to oxygen atoms, adsorbed carbonates, and π-π satellite, respectively [20,21,23]. Peaks at 284.5–284.0 (asymmetric) and 285.2 eV (Gaussian) were attributed in the literature [21,22] to sp2-hybridized graphite-like C atoms and sp3 C atoms no longer in the regular tubular structure, respectively. Unfortunately, the vast majority of surfaces following air exposure, as is the case of our samples, get contaminated with very small amounts of adventitious carbon which dramatically affect the interpretation of the latter peaks [24]. Consequently, any attempt to herein quantify the sp2:sp3 C ratio may be subjected to important errors. Deconvolution of pCNT O1s peak shows mainly the contribution of a broad band at 533.1 eV and two minor contributions with BE of 531.9 and 534.8 eV, respectively, see S.D. XPS. Contributions at 531.9 and 533.1 eV confirmed the presence of hydroxyl and carboxylic functions onto the pCNT surface, respectively [20]. Contributing peaks to the C1s and O1s XPS signals of iCNT are similar to those observed for pCNT. The percent
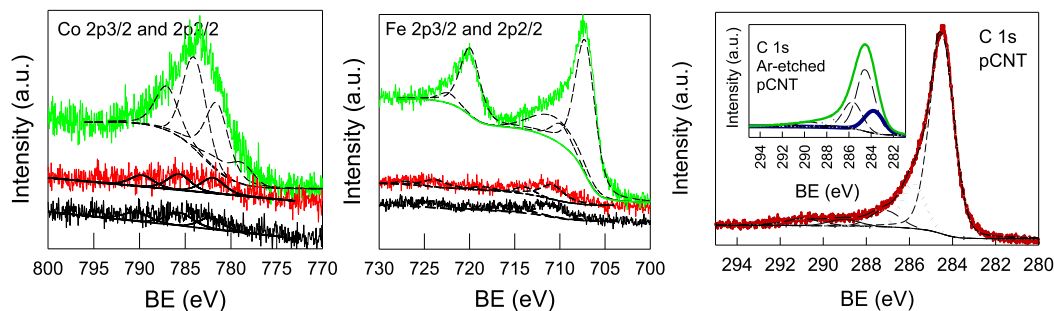
Fig. 4. Co 2p3/2, Fe 2p3/2, and C1s XPS peaks observed for: pCNT (black lines), iCNT (red lines), and argon etching of pCNT (green lines). Black dashed line curves represent the components obtained from the deconvolution of the peaks, as explained in the text. The C1s peak of argon etched pCNT shows the peak at 284.0 eV in blue. (A colour version of this figure can be viewed online.)

contribution for C1s signals for as obtained, Ar-bombarded, and irradiated samples are depicted in S.D. XPS Table 1.

Interestingly, argon etched pCNT show the contributions already described for pCNT as well as a new peak at 284.0 eV, see Fig. 4, which may be assigned to sp2 C [21] and/or to amorphous C on a Ni surface [20] in line with the fact that Ar etching exposes the interior tubes of MWCNT and Ni impurities.

Considering the experimental sensitivity factors of the different elements, and the areas below all signals, except for the contribution of the signal at 284.6 eV, the average surface composition of pCNT, iCNT, and Ar-bombarded pCNT are estimated as $C_1O_{1.25}Fe_{0.013}Co_{0.008}$, $C_1O_{0.98}Fe_{0.014}Co_{0.007}$, and $C_1O_{0.07}Fe_{0.5-}Co_{0.2}Ni_{0.2}$, respectively. Since Ar-etching decreases the thickness of the original nanotubes, XPS signals from both, the oxidized and amorphous carbon and the virgin nanotubes from below overlap. Consequently, an important reduction in the oxygen content and an important increase in metal catalysts in inner tubes is observed. On the other hand, a 20% decrease in the oxygen content of surface functionalities and an unmodified residual metal content was observed after 350 nm photolysis of pCNT.

pCNT treatment with HCl and further analysis of the filtered solution by ICP, see experimental section, shows the presence of 2.9×10^{-5}, 4.94×10^{-5}, and 1.5×10^{-3} mol of Co, Fe, and Al, respectively, per g of pCNT inside accessible sites to HCl. The fact that Ni was not observed in the filtrate and that HCltCNT still show magnetic properties (see S.D. Magnetization curves) strongly support that mainly externally located surface metals are accessible to mild acid treatment. Aluminum is the most abundant metal (>75% of total metals) probably present as a free residue. Also, TEM micrographs of HCltCNTs still show that amorphous materials remain after HCl treatment, see S.D. TEM.

The attenuance spectrum of pCNT and iCNT (10 ppm analytical concentration) in aqueous suspensions (Fig. 5) increases monotonously with decreasing wavelength in the range from 400 to 800 nm and show a broad absorption peak *ca.* 270 nm attributed to π-π* optical transitions [23]. π-plasmon resonance transitions dominate the high-energy part of the spectrum and extends into the far-IR [25]. However, the contribution of non-nanotube carbonaceous impurities to π-plasmon absorption, as reported for single-wall CNT, cannot be discarded [25,26]. iCNT shows a lower overall attenuance than pCNT in aqueous suspensions. Sodium Dodecyl Sulfate (SDS) was added to both pCNT and iCNT suspensions to improve the dispersibility of MWCNT [27]. iCNT suspensions with added 6 μM SDS and further 20 min sonication show higher overall attenuance than equally treated pCNT (see Fig. 5 *inset*), thus suggesting that iCNT surface is more hydrophobic than that of pCNT.

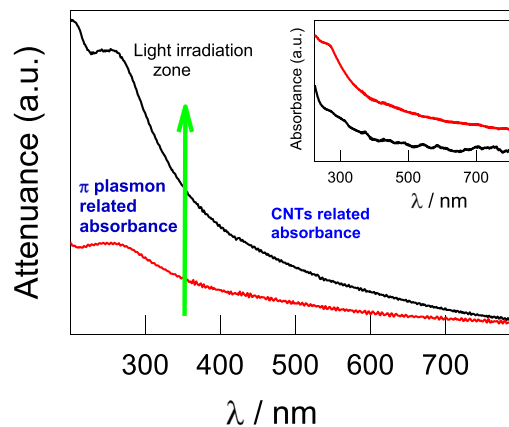Altogether, the above results indicate that 350 nm photolysis of

Fig. 5. Absorption spectra of an aqueous suspension of 10 ppm analytical concentration of pCNT (black curve) and iCNT (red curve). The green arrow stands for the irradiation wavelength. *Inset:* Absorption spectra of an aqueous suspension of 10 ppm analytical concentration of pCNT (black curve) and iCNT (red curve) also containing 6mM SDS. (A colour version of this figure can be viewed online.)

pCNT leads to iCNT with less disordered carbon structures (as indicated by Raman) and with lower content of oxidized surface groups (as supported by XPS and FTIR). These observations are in line with the more difficult to oxidize carbon structures and the lower dispersibility observed after photolysis (as suggested by TGA and UV-vis spectroscopy, respectively). Photoinduced formation of highly ordered graphitic material (observed by HRTEM) is suggested to arise from broken pCNT walls. However, since photolysis does not significantly remove synthesis residual metals (as indicated by XPS data), extensive MWCNT pealing does not take place. These observations are in line with literature reports on the continuous 1064 nm laser light radiation showing C−C bonds breaking and formation of new graphene layers on a silica surface which was attributed to the light-induced temperature raise which in turn prompts the occurrence of chemical reactions [28].

3.2. Time resolved experiments with pulsed lasers

Irradiation with 355 nm laser light was performed to observe the nature of photogenerated transients. Comparison of the transients formed after irradiation of pCNT, iCNT, and HCltCNT depicted in Fig. 6 brings some understanding on the effect of surface defects and residual metals on the photophysics of MWCNT.

During the nanosecond laser pulse, all signals are dominated by photobleaching, similar to that shown for HCltCNT in Fig. 6A. In
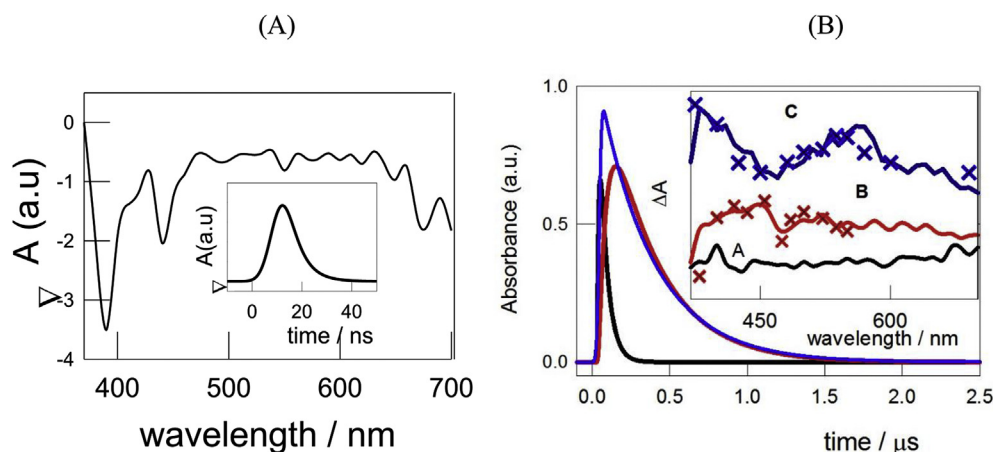
(A)   (B)

Fig. 6. Transients observed after 355 nm irradiation with a laser flash of aqueous suspensions of: (A) HCltCNT (black lines); (B) pCNT transient A (black line) and transient B (red line), iCNT transient C (blue lines). Blue crosses stand for the normalized sum of reported SWCNT$^{\bullet-}$ and SWCNT$^{\bullet+}$ transient spectra and red crosses stand for the sum of SWCNT$^{\bullet-}$ and the radical cation spectra of resorcinol and catechol. (A colour version of this figure can be viewed online.)

fact, none of the samples showed photoluminescence, in agreement with the expectation that the optical excitation and emission of semiconducting shells would decay non-radiatively in the presence of adjacent shells with metallic character. After photobleaching, pCNT depict the consecutive formation and decay of two transient species with 49 and 321 ns decay lifetimes and absorption spectra depicted in Fig. 6B. On the other hand, iCNT mainly show the formation of one transient after photobleaching with decay times of 337 ns and absorption spectra shown by the blue traces in Fig. 6B. HCltCNT show bleaching and no subsequent transient formation in our experimental time window.

The formation of excitons by the direct photoexcitation of semiconducting MWCNTs is observed as the initial short-lived bleaching bands shown in Fig. 6A, in agreement with the reported photobleaching of SWCNTs in deaerated DMF [29] taking place before the photoinduced electron transfer from SWNT to acceptors. Interestingly, the effect of single or multiple wall structure of the nanotubes or the predominant location of acceptor groups is reported to play a minor role in the photochemical event in the nanosecond or higher time scale [30]. Therefore, comparison of transient spectra obtained here with those reported for SWCNT seems reasonable.

The structureless transient absorption spectrum consisting in a broad band spanning the 370–800 nm wavelength range formed following the initial photobleaching of pCNTs (see black curve in Fig. 6B, denoted as transient "A") resembles that reported in the literature for the single transient formed after 355 nm laser irradiation of SWCNT acetonitrile suspensions [31]. On the other hand, transients with an absorption band appearing in the 360–450 nm range (see red curve in Fig. 6B, denoted as transients "B") show absorption in the same wavelength range than positive electron holes on MWCNT [30,31]. However, the matching between obtained and reported MWCNT$^{\bullet+}$ spectrum is not good. In fact, transients with maximum absorption between 400 and 450 nm resemble those of phenolic radical cations which lifetimes in organic solvents is in the range of the hundreds of ns [32,33], in line with our observations. On the other hand, the broad absorbance between 490 and 580 nm is very similar to that attributed to a delocalized SWCNT$^{\bullet-}$ radical anion in organic solvent suspensions [34–36]. Taking the linear combination of reported radical cation spectra for resorcinol and catechol [32,33] and that of SWCNT$^{\bullet-}$ [34–36], the resulting overall spectrum is in good agreement with that observed experimentally for transients "B" (see red crosses in

Fig. 6B *inset*). Thus, 355 nm laser irradiation of iCNT leads to an efficient e$^-$ ⁻ h$^+$ charge separated state with decay lifetimes in the range of 350 ns. Since oxygen-containing surface groups are ubiquitous at the edges and mid-zone of the graphene walls of MWCNTs and in amorphous carbon impurities, these surface functionalities might be responsible for much of the chemical reactivity of CNTs as sp2 hybridized C atoms at the planes with a delocalized π electron system are much less reactive. Therefore, the contribution of phenolic type radical cations present as amorphous carbon or oxidized surface functionalities cannot be discarded.

The transient formed after iCNTs photolysis shows a broad absorbance between 490 and 580 nm which is very similar to that attributed to a delocalized SWCNT$^{\bullet-}$ radical anion in organic solvent suspensions [34–36]. On the other hand, transient absorption in the wavelength range from 370 to 450 nm resembles that of SWCNT$^{\bullet+}$ radicals [30,31]. The good coincidence of the observed transient absorption with the linear combination of SWCNT$^{\bullet-}$ and SWCNT$^{\bullet+}$ spectra reported by different authors is also shown in Fig. 6B *inset*. Thus, 355 nm laser irradiation of iCNT leads to an efficient e$^-$ ⁻ h$^+$ charge separated state with decay lifetimes in the range of 350 ns. Both transients are denoted as transients "C." However, the peak at 560 nm is still unassigned.

HCltCNT with minimized external adsorbed metals do not generate, within the experimental error, MWCNT radical transients upon 355 nm irradiation. HCl-treatment of MWCNT was also reported to cause a significant decrease of oxygen bonded to disordered carbon [21]. Therefore, remnant metal catalysts and oxygen containing amorphous carbon must play an important role in the generation of MWCNT photoinduced charge-separated states. In fact, heptagon defect pairs in double walled carbon nanotubes, DWCNT, tips and curvatures, carbon-oxygen functionalities on DWCNTs surface and edges, and catalyst impurities have also been proposed as the active sites for the improved activation behavior reported for the electro reduction of O$_2$ to H$_2$O$_2$ by DWCNT-modified electrodes [37].

According to the previous evidence, a possible reaction mechanism taking place upon 350–355 nm irradiation of pCNT aqueous suspensions is shown in Fig. 7. Photoexcitation of pCNT with 355 nm light leads to the formation of MWCNT excitons (transient A in reaction (1)) which subsequently may undergo MWCNT hole transfer to attached external metal impurities forming a charge separation state (transient B in reaction (2)), in agreement with the reported mechanism taking place upon excitation of Fe$_2$O$_3$/CNT and

$$\text{pCNT/RI} + h\nu\ (355\ nm) \rightarrow (e^- - h^+)\text{pCNT/RI} \qquad\qquad \textit{exciton formation} \qquad (1)$$

$$(e^- - h^+)\text{pCNT/RI} \rightarrow \text{pCNT/RI} + \text{heat or light} \qquad\qquad \textit{exciton recombination} \quad (-1)$$

$$(e^- - h^+)\text{pCNT/RI} \rightarrow (e^-)\text{pCNT/RI}(h^+) \qquad\qquad \textit{charge separated state} \quad (2)$$

$$(e^-)\text{pCNT/RI}(h^+) + O_2 \rightarrow (O_2{}^{\bullet-})\text{pCNT/RI}(h^+) \qquad\qquad \textit{adsorbed superoxide formation} \quad (3)$$

$$(O_2{}^{\bullet-})\text{pCNT/RI}(h^+)) \rightarrow H_2O_2 + \text{pCNT/RI}(h^+) \qquad \textit{adsorbed superoxide recombination} \quad (4)$$

$$(e^-)\text{pCNT/RI}(h^+)) \rightarrow Ox^- + {}^{\bullet}\text{CNT/RI}(h^+) \qquad \textit{MWCNT}^{\bullet-}\ \textit{reactions on oxidized edges} \quad (5)$$

$$\text{pCNT/RI}(h^+) \rightarrow \text{pCNT/RIoxidized} \qquad\qquad \textit{hole oxidation of amorphous carbon} \quad (6)$$
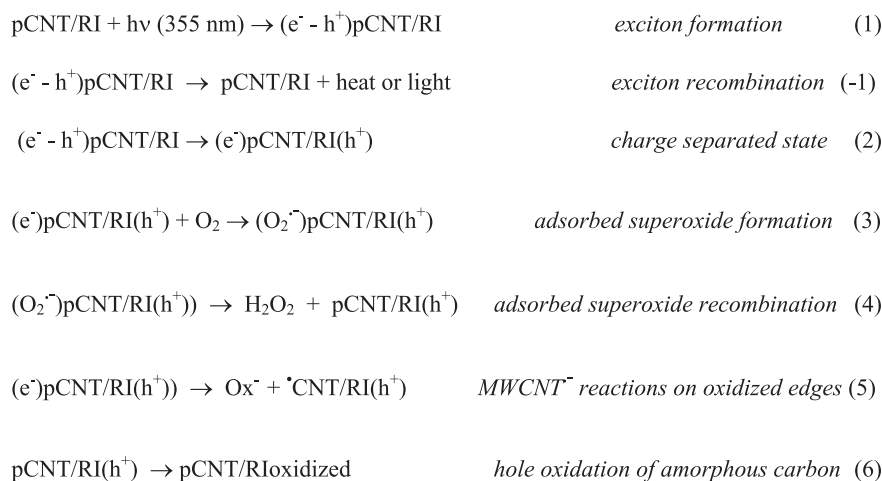
Fig. 7. Proposed reaction mechanism taking place after 350—355 nm irradiation of pCNT aqueous suspensions. RI stands for residual impurities as Fe oxides and amorphous C attached to pCNT (pCNT/RI), h^+ and e^- for photogenerated holes and electrons, respectively, and Ox^- for oxidized molecules such as enolates.

TiO_2/CNT semiconductor assemblies [38]. Otherwise it may recombine, reaction (-1), liberating heat or emitting light. Fast recombination, seems to be the main decay mechanism for HCltCNT excitons.

Under oxygen saturation, $SWCNT^{\bullet-}$ radical anions are expected to efficiently react with O_2 to yield $O_2{}^{\bullet-}$, reaction (3). However, $O_2{}^{\bullet-}$ was not detected in continuous irradiation EPR experiments but its recombination product, H_2O_2, was observed to be formed in appreciable amounts (pCNT show estimated [H_2O_2] of 15 mM/h and iCNTs show seven-fold times higher concentration of *ca.* 103 mM/h). An efficient $O_2{}^{\bullet-}$ recombination on MWCNT surface, reaction (4) significantly competing with the solution reaction between $O_2{}^{\bullet-}$ and the trapping agent might be the cause impeding its detection by EPR. These observations are in line with literature reports indicating that free radicals are not observed in the presence of H_2O_2 and that MWCNT rather exhibit radical scavenging capacity when in contact with an external source of hydroxyl or superoxide radicals [39,40].

It should be recalled that the term pCNT also considers carbon-oxygen functionalities on MWCNT surface and edges. Radical anions of surface oxidized $SWCNT^{\bullet-}$ may lead to the elimination of oxidized molecules and formation of radicals on the MWCNT surface, denoted as $^{\bullet}$MWCNT radicals, reaction (5), in line with reported reactions of substituted aromatic radical anions [41—43] and the detection by EPR of $RCH_2{}^{\bullet}$ radicals in irradiation experiments of pCNT aqueous suspensions (see S.D. EPR). Reaction (6) shows the scavenging of holes on the metal oxides by amorphous carbon.

Reactions (5) and (6) removing oxidized surface groups and amorphous C present in the form of chains or disordered clusters causes the reduction of Raman A_D/A_G ratio observed for pCNT after photolysis. These reactions are consistent with the lower content of oxidized surface groups observed for iCNT by XPS and FTIR. The occurrence of multiple reactions of the type shown in (5) and (6) is a possible mechanism leading to the breakdown and stripping of the outer walls, in line with literature reports on C radicals on the carbon nanotubes which were considered to be responsible for the modification of the MWCNT structures and the formation of new carbon nanostructures [44].

A similar reaction scheme might apply to iCNT. The difference in the transient nature of the charge separated state (reaction (2)) observed for pCNT and iCNT, is evidently related to the oxygen content in amorphous and MWCNTs graphene edge and mid-zones of each sample. Formation of graphite and probably graphene sheets in contact with metal impurities may act as hole acceptors in the charge separated state after 355 nm photolysis of iCNT.

4. Conclusions

Several techniques including HRTEM, XPS, Raman, TGA, and EPR spectroscopy, among others, were used in combination with steady state photolysis and transient absorption spectroscopy to elucidate the reaction mechanisms and morphology changes taking place upon 350—355 nm light irradiation of as obtained commercial MWCNT. We demonstrated that residual metal catalysts and oxygen containing amorphous carbon located in external MWCNT sites and oxidized C-functionalities of MWCNT play an important role in the generation of MWCNT photoinduced charge-separated states. As also discussed in the literature for SWCNT, hole transfer to metal oxides and further reaction with oxidized functionalities seems to be the preferred reaction mechanism. As a consequence of the photoinduced process, fragmentation of oxidized moieties and generation of $^{\bullet}$MWCNT radicals takes place. Finally, the photoinduced breakage of oxidized walls leads to the exposure of less oxidized inner walls.

The information herein obtained is of importance for massive technological uses of MWCNT were residual impurities from the synthesis procedure may have unexpected consequences. Also, the observed photoinduced processes may be used for the development of new technological uses of as obtained MWCNT.

Appendix A. Supplementary data

Supplementary data related to this article can be found at https://doi.org/10.1016/j.carbon.2018.05.078.

References

[1] C.E. Banks, A. Crossley, C. Salter, S.J. Wilkins, R.G. Compton, Carbon nanotubes contain metal impurities which are responsible for the "electrocatalysis" seen at some nanotube-modified electrodes, Angew. Chem. Int. Ed. 45 (2006) 2533—2537, https://doi.org/10.1002/anie.200600033.

[2] A. Salehi-Khojin, F. Khalili-Araghi, M.A. Kuroda, K.Y. Lin, J.P. Leburton, R.I. Masel, On the sensing mechanism in carbon nanotube chemiresistors, ACS Nano 5 (2011) 153—158, https://doi.org/10.1021/nn101995f.

[3] A. Eatemadi, H. Daraee, H. Karimkhanloo, M. Kouhi, N. Zarghami, A. Akbarzadeh, M. Abasi, Y. Hanifehpour, S.W. Joo, Carbon nanotubes: properties, synthesis, purification, and medical applications, Nanoscale Res Lett. 9 (2014) 1—13, https://doi.org/10.1186/1556-276X-9-393.

[4] A. Falqui, D. Loche, M.F. Casula, A. Corrias, D. Gozzi, A. Latini, Synthesis and characterization of multiwalled carbon nanotube/FeCo nanocomposites, J. Nanosci. Nanotechnol. 11 (2011) 2215—2225, https://doi.org/10.1166/jnn.2011.3725.

[5] C.H.A. Wong, Z. Sofer, M. Kubešova, J. Kučera, S. Matějkova, M. Pumera, Së, Proc. Natl. Acad. Sci. 111 (2014) 13774—13779, https://doi.org/10.1073/pnas.1413389111.

[6] B. Sljukić, C.E. Banks, R.G. Compton, Iron oxide particles are the active sites for hydrogen peroxide sensing at multiwalled carbon nanotube modified electrodes, Nano Lett. 6 (2006) 1556—1558, https://doi.org/10.1021/nl060366v.

[7] L. Bokobza, J. Zhang, Raman spectroscopic characterization of multiwall carbon nanotubes and of composites, Express Polym. Lett. 6 (2012) 601—608, https://doi.org/10.3144/expresspolymlett.2012.63.

[8] L. Zhang, H. Li, K.-T. Yue, S.-L. Zhang, X. Wu, J. Zi, Z. Shi, Z. Gu, Effects of intense laser irradiation on Raman intensity features of carbon nanotubes, Phys. Rev. B 65 (2002) 10—13, https://doi.org/10.1103/PhysRevB.65.073401.

[9] Á. Pérez Del Pino, E. György, L. Cabana, B. Ballesteros, G. Tobias, Ultraviolet pulsed laser irradiation of multi-walled carbon nanotubes in nitrogen atmosphere, J. Appl. Phys. 115 (2014) 1—10, https://doi.org/10.1063/1.4864776.

[10] C. Mikó, M. Milas, J.W. Seo, R. Gaál, A. Kulik, L. Forró, Effect of ultraviolet light irradiation on macroscopic single-walled carbon nanotube bundles, Appl. Phys. Lett. 88 (2006), https://doi.org/10.1063/1.2195013.

[11] J.J. Snellenburg, S.P. Laptenok, R. Seger, K.M. Mullen, I.H.M. van Stokkum, Glotaran: a java -based graphical user interface for the R Package TIMP, J. Stat. Softw. 49 (2012), https://doi.org/10.18637/jss.v049.i03.

[12] M. Zdrojek, W. Gebicki, C. Jastrzebski, T. Melin, A. Huczko, Studies of multiwall carbon nanotubes using Raman spectroscopy and atomic force microscopy, Solid State Phenom. 99—100 (2004) 265—268, https://doi.org/10.4028/www.scientific.net/SSP.99-100.265.

[13] S. Osswald, E. Flahaut, H. Ye, Y. Gogotsi, Elimination of D-band in Raman spectra of double-wall carbon nanotubes by oxidation, Chem. Phys. Lett. 402 (2005) 422—427, https://doi.org/10.1016/j.cplett.2004.12.066.

[14] J.H. Lehman, M. Terrones, E. Mansfield, K.E. Hurst, V. Meunier, Evaluating the characteristics of multiwall carbon nanotubes, Carbon N. Y. 49 (2011) 2581—2602, https://doi.org/10.1016/j.carbon.2011.03.028.

[15] N. Chakrapani, S. Curran, B. Wei, P.M. Ajayan, A. Carrillo, R.S. Kane, Spectral fingerprinting of structural defects in plasma-treated carbon nanotubes, J. Mater. Res. 18 (2003) 2515—2521, https://doi.org/10.1557/JMR.2003.0350.

[16] C.M. White, R. Banks, I. Hamerton, J.F. Watts, Characterisation of commercially CVD grown multi-walled carbon nanotubes for paint applications, Prog. Org. Coatings 90 (2016) 44—53, https://doi.org/10.1016/j.porgcoat.2015.09.020.

[17] F. Avilés, J.V. Cauich-Rodríguez, L. Moo-Tah, A. May-Pat, R. Vargas-Coronado, Evaluation of mild acid oxidation treatments for MWCNT functionalization, Carbon N. Y. 47 (2009) 2970—2975, https://doi.org/10.1016/j.carbon.2009.06.044.

[18] L. Liu, D. Wang, Y. Hu, Self-assembly fabrication of a graphene/multi-walled carbon nanotube hybrid material for suppressing potential heat radiation and toxic effluent, RSC Adv. 5 (2015) 103365—103372, https://doi.org/10.1039/C5RA19227G.

[19] D. Tang, J. Su, Q. Yang, M. Kong, Z. Zhao, Y. Huang, X. Liao, Y. Liu, Preparation of alumina-coated graphite for thermally conductive and electrically insulating epoxy composites, RSC Adv. 5 (2015) 55170—55178, https://doi.org/10.1039/C5RA08010J.

[20] Nist, NIST X-ray Photoelectron Spectroscopy Database, Version 4.1, National Institute of Standards and Technology, Gaithersburg, 2012 (2012), http://srdata.nist.gov/xps/.

[21] V. Datsyuk, M. Kalyva, K. Papagelis, J. Parthenios, D. Tasis, A. Siokou, I. Kallitsis, C. Galiotis, Chemical oxidation of multi-walled carbon nanotubes, Carbon N. Y. 46 (2008) 833—840, https://doi.org/10.1016/j.carbon.2008.02.012.

[22] H. Ago, T. Kugler, F. Cacialli, W.R. Salaneck, M.S.P. Shaffer, A.H. Windle, R.H. Friend, Work functions and surface functional groups of multiwall carbon nanotubes, J. Phys. Chem. B 103 (1999) 8116—8121, https://doi.org/10.1021/jp991659y.

[23] H. Ago, T. Kugler, F. Cacialli, W.R. Salaneck, M.S.P. Shaffer, A.H. Windle, R.H. Friend, Work functions and surface functional groups of multiwall carbon nanotubes, J. Phys. Chem. B 103 (1999) 8116—8121, https://doi.org/10.1021/jp991659y.

[24] G. Greczynski, L. Hultman, C 1s peak of adventitious carbon aligns to the vacuum level: dire consequences for Material's bonding assignment by photoelectron spectroscopy, ChemPhysChem 18 (2017) 1507—1512, https://doi.org/10.1002/cphc.201700126.

[25] M.E. Itkis, D.E. Perea, R. Jung, S. Niyogi, R.C. Haddon, Comparison of analytical techniques for purity evaluation of single-walled carbon nanotubes, J. Am. Chem. Soc. 127 (2005) 3439—3448, https://doi.org/10.1021/ja043061w.

[26] B. Zhao, M.E. Itkis, S. Niyogi, H. Hu, J. Zhang, R.C. Haddon, Study of the extinction coefficients of single-walled carbon nanotubes and related carbon materials, J. Phys. Chem. B 108 (2004) 8136—8141, https://doi.org/10.1021/jp037402o.

[27] R. Rastogi, R. Kaushal, S.K. Tripathi, A.L. Sharma, I. Kaur, L.M. Bharadwaj, Comparative study of carbon nanotube dispersion using surfactants, J. Colloid Interface Sci. 328 (2008) 421—428, https://doi.org/10.1016/j.jcis.2008.09.015.

[28] Y. Yuan, J. Chen, Nano-welding of multi-walled carbon nanotubes on silicon and silica surface by laser irradiation, Nanomaterials 6 (2016) 36, https://doi.org/10.3390/nano6030036.

[29] M. Ohtani, S. Fukuzumi, Solubilization and photoinduced electron transfer of single-walled carbon nanotubes wrapped with coenzyme Q(10), Chem. Commun. (Camb) (2009) 4997—4999, https://doi.org/10.1039/b910080f.

[30] R. Martín, F.J. Céspedes-Guirao, M. de Miguel, F. Fernández-Lázaro, H. García, Á. Sastre-Santos, Single- and multi-walled carbon nanotubes covalently linked to perylenebisimides: synthesis, characterization and photophysical properties, Chem. Sci. 3 (2012) 470—475, https://doi.org/10.1039/C1SC00609F.

[31] M. Alvaro, C. Aprile, B. Ferrer, H. Garcia, Functional molecules from single wall carbon nanotubes. Photoinduced solubility of short single wall carbon nanotube residues by covalent anchoring of 2,4,6-triarylpyrylium units, J. Am. Chem. Soc. 129 (2007) 5647—5655, https://doi.org/10.1021/ja0690520.

[32] O. Brede, S. Kapoor, T. Mukherjee, R. Hermann, S. Naumov, Diphenol radical cations and semiquinone radicals as direct products of the free electron transfer from catechol, resorcinol and hydroquinone to parent solvent radical cations, Phys. Chem. Chem. Phys. 4 (2002) 5096—5104, https://doi.org/10.1039/b205771a.

[33] R. Joshi, S. Naumov, S. Kapoor, T. Mukherjee, R. Hermann, O. Brede, Phenol radical cations and phenoxyl radicals in electron transfer from the natural phenols sesamol, curcumin and trolox to the parent radical cations of 1-chlorobutane, J. Phys. Org. Chem. 17 (2004) 665—674, https://doi.org/10.1002/poc.836.

[34] M. Alvaro, P. Atienzar, P. De La Cruz, J.L. Delgado, H. Garcia, F. Langa, Sidewall functionalization of single-walled carbon nanotubes with nitrile imines. Electron transfer from the substituent to the carbon nanotube, J. Phys. Chem. B 108 (2004) 12691—12697, https://doi.org/10.1021/jp0480044.

[35] M. Álvaro, P. Atienzar, J.L. Bourdelande, H. García, An organically modified single wall carbon nanotube containing a pyrene chromophore: Fluorescence and diffuse reflectance laser flash photolysis study, Chem. Phys. Lett. 384 (2004) 119—123, https://doi.org/10.1016/j.cplett.2003.12.010.

[36] D.M. Guldi, M. Marcaccio, D. Paolucci, F. Paolucci, N. Tagmatarchis, D. Tasis, E. Vázquez, M. Prato, Single-wall carbon nanotube-ferrocene nanohybrids: observing intramolecular electron transfer in functionalized SWNTs, Angew. Chem. Int. Ed. 42 (2003) 4206—4209, https://doi.org/10.1002/anie.200351289.

[37] I. Kruusenberg, L. Matisen, H. Jiang, M. Huuppola, K. Kontturi, K. Tammeveski, Electrochemical reduction of oxygen on double-walled carbon nanotube modified glassy carbon electrodes in acid and alkaline solutions, Electrochem. Commun. 12 (2010) 920—923, https://doi.org/10.1016/j.elecom.2010.04.021.

[38] W.-D. Zhang, B. Xu, L.-C. Jiang, Functional hybrid materials based on carbon nanotubes and metal oxides, J. Mater. Chem. 20 (2010) 6383, https://doi.org/10.1039/b926341a.

[39] S. Tsuruoka, H. Matsumoto, K. Koyama, E. Akiba, T. Yanagisawa, F.R. Cassee, N. Saito, Y. Usui, S. Kobayashi, D.W. Porter, V. Castranova, M. Endo, Radical scavenging reaction kinetics with multi-walled carbon nanotubes, Carbon N Y. 83 (2015) 232—239, https://doi.org/10.1016/j.carbon.2014.10.009.

[40] I. Fenoglio, M. Tomatis, D. Lison, J. Muller, A. Fonseca, J.B. Nagy, B. Fubini, Reactivity of carbon nanotubes: free radical generation or scavenging activity? Free Radic. Biol. Med. 40 (2006) 1227—1233, https://doi.org/10.1016/j.freeradbiomed.2005.11.010.

[41] R.D. Guthrie, M. Patwardhan, J.E. Chateauneuf, Cleavage rates for radiolysis-produced radical anions of naphthylmethyl phenyl ethers, J. Phys. Org. Chem. 7 (1994) 147—152.

[42] N.L. Holy, Reactions of the radical anions and dianions of aromatic hydrocarbons, Chem. Rev. 74 (1974) 243—277, https://doi.org/10.1021/cr60288a005.

[43] J. Masnovi, Radical anions of esters of carboxylic acids. Effects of structure and solvent on unimolecular fragmentations, J. Am. Chem. Soc. 111 (1989) 9081—9089, https://doi.org/10.1021/ja00207a014.

[44] G. Yu, J. Gong, S. Wang, D. Zhu, S. He, Z. Zhu, Etching effects of ethanol on multi-walled carbon nanotubes, Carbon N Y. 44 (2006) 1218—1224, https://doi.org/10.1016/j.carbon.2005.10.050.